6-6-2012

Ionospheric Plasma Transport and Loss in Auroral Downward Current Regions

M. Zettergren
Embry-Riddle Aeronautical University, zettergm@erau.edu

J. L. Semeter
Boston University

Scholarly Commons Citation

Zettergren, M., and J. Semeter (2012), Ionospheric plasma transport and loss in auroral downward current regions,J. Geophys. Res.,117, A06306.

Ionospheric plasma transport and loss in auroral downward current regions

M. Zettergren[1] and J. Semeter[2]

Received 20 February 2012; revised 2 April 2012; accepted 18 April 2012; published 6 June 2012.

[1] A detailed study of the effects of auroral current systems on thermal ionospheric plasma transport and loss is conducted using a new ionospheric model. The mathematical formulation of the model is a variation on the 5-moment approximation which describes the temporal evolution of density, drift, and temperature for five different ion species in two spatial dimensions. The fluid system is closed through a 2-D electrostatic treatment of the auroral currents. This model is used to examine the interplay between ion heating, perpendicular transport, molecular ion generation, and type-1 ion upflows in a self-consistent way for the first time. Simulations confirm that the depletion of E-region plasma due to current closure occurs on extremely fast time scales (5–30 s), and that it is dependent on current system scale size. Near the F-region peak, the loss is mostly due to enhanced recombination from the conversion of the plasma to molecular ions. The F-region loss process is fairly slow (120–300 s) by comparison to lower altitude processes and is highly electric field dependent. On similar time scales, transient ion upflows from frictional heating move plasma from the near topside ionosphere (∼500 km) to higher regions, leaving depletions and enhancing plasma densities at very high altitudes. Results indicate the existence of large molecular ion upflows near the F-region peak and may shed some light on ionospheric source regions for outflowing molecular ions. Neutral atmospheric winds and densities are also shown to play an important role in modulating molecular ion densities, frictional heating, and currents.

Citation: Zettergren, M., and J. Semeter (2012), Ionospheric plasma transport and loss in auroral downward current regions, *J. Geophys. Res.*, *117*, A06306, doi:10.1029/2012JA017637.

1. Introduction

[2] A wide variety of transport and chemical processes affect the distribution of ionospheric plasma in auroral current systems. Ionospheric plasma depletions are commonly observed by incoherent scatter radars (ISRs) in the E- and F-regions adjacent to auroral arcs [*Doe et al.*, 1993; *Aikio et al.*, 2004]. The formation of these depletions is, at least partly, a consequence of maintaining current continuity through the ionospheric regions [*Doe et al.*, 1995; *Streltsov and Lotko*, 2008]. In a typical auroral system, the field-aligned currents are carried by electrons, while the current is closed through the E-region by ion motions perpendicular to the geomagnetic field. The downward current region (DCR) is necessarily subjected to a plasma loss due the closure of auroral currents since ions (moving from DCR to upward current region) and electrons (moving upward to carry the downward current) are leaving this region. As the DCR is depleted of charge carriers, current continuity is maintained on longer time scales by broadening of the downward current channel [*Cran-McGreehin et al.*, 2007] or by accessing charge carriers from the *F*-region, thus depleting the lower *F*-region, as well [*Doe et al.*, 1995; *Karlsson et al.*, 2005]. In a large scale downward current, conditions are favorable for the ionospheric feedback instability [*Lysak and Song*, 2002] which involves reflection of small-scale Alfvén waves back toward the magnetosphere and possible wave trapping in the ionospheric Alfvén resonator [e.g., *Streltsov and Lotko*, 2004]. Modeling of this process has shown that in severe cases the intensity of the trapped waves is sufficient to produce a ponderomotive force capable of almost completely evacuating the lower *F*-region of the ionosphere [*Streltsov and Lotko*, 2008].

[3] Intense perpendicular electric fields are ubiquitous features of auroral currents systems [*Marklund*, 1984; *Johnson et al.*, 1998], and are often localized near the arc boundaries [e.g., *Evans et al.*, 1977; *Opgenoorth et al.*, 1990; *de La Beaujardiere et al.*, 1977]. Ion frictional heating by these fields speeds the conversion of F-region O^+ into NO^+ [*McFarland et al.*, 1973; *Torr et al.*, 1977; *St.-Maurice and Torr*, 1978; *St.-Maurice and Laneville*, 1998] and results

[1]Physical Sciences Department, Embry-Riddle Aeronautical University, Daytona Beach, Florida, USA.
[2]Department of Electrical and Computer Engineering and Center for Space Physics, Boston University, Boston, Massachusetts, USA.

Corresponding author: M. Zettergren, Physical Sciences Department, Embry-Riddle Aeronautical University, 600 S. Clyde Morris Blvd., Daytona Beach, FL 32114, USA. (zettergm@erau.edu)

0148-0227/12/2012JA017637

in enhanced recombination loss, since the molecular ions have shorter chemical lifetimes. Various indirect ISR measurements of this process have suggested that a substantial fraction of the F-region can be molecular during strong electric fields [*Kelly and Wickwar*, 1981; *Haggstrom and Collis*, 1990; *Lathuillère and Kofman*, 2006; *Zettergren et al.*, 2011], and these observations are corroborated in a few theoretical studies [*Schunk et al.*, 1975; *Diloy et al.*, 1996]. Generally speaking, electric fields which initiate the ion heating are strongest in the DCR, so it would seem that both the current closure and recombination loss processes are likely to occur in this region [*Zettergren et al.*, 2010].

[4] In addition to perpendicular transport, which initiates the plasma redistribution/loss processes discussed above, field-aligned thermal ion upflows are a common feature of strong auroras. In contrast with the polar wind [*Banks and Holzer*, 1969; *Ganguli*, 1996], auroral zone ion upflow is produced by processes that deposit electromagnetic and kinetic energy directly into the *E*- and *F*-regions of the ionosphere. The frictional heating process discussed previously will also produce expansion and upflow (type-1 upflow [e.g., *Wahlund et al.*, 1992]). In the auroral zone, often near the polar cap boundary or cusp regions, soft particle precipitation heats the ambient ionospheric electrons and causes field-aligned ambipolar plasma flows (type-2 upflow [e.g., *Richards*, 1995]). At altitudes above where upflows are initiated, transverse plasma waves can energize ions perpendicular to the magnetic field, and the mirror force can then propel them to escape velocity ('ion outflow') [e.g., *André et al.*, 1998]. Finally, parallel electric fields associated with the auroral acceleration region can produce outflowing ions in the form of ion beams [*McFadden et al.*, 1998]. Recent measurements seem to suggest that both the upflow and outflow processes work in concert to transport ionospheric heavy ions into the magnetosphere [*Lynch et al.*, 2007; *Ogawa et al.*, 2008]. For a more complete account of the upflow/outflow process see reviews by *André and Yau* [1997], *Yau and André* [1997], *Moore et al.* [1999], and *Moore and Horwitz* [2007] and references therein.

[5] For the present work, we restrict our attention to plasma loss and transport processes which are prominent in auroral downward current regions - current closure plasma loss, frictional heating, enhanced recombination, and type-1 upflows. The general morphology of auroral arcs (i.e., strong electric fields in DCRs) suggests that all of these processes should be important to the dynamics of the ionospheric plasma in DCRs. Even so, to date there appears to be no comprehensive, systematic study of how these diverse and collocated processes interact to produce observed plasma depletions and upflows. In this research we develop a new 2-D numerical ionospheric model which is able to self-consistently describe plasma transport and loss in auroral downward current regions. This model is used to examine the coupled effects of these processes and assess their relative importance in producing observed plasma structure. An additional motivation for the development of such a code is the deployment of new phased-array incoherent scatter radars which are capable of providing improved ionospheric diagnostics in the form of two-dimensional and volumetric observations [*Semeter et al.*, 2009, 2010; *Butler et al.*, 2010]. The availability of such data sets necessitates development of detailed two and three-dimensional models for quantitative comparisons.

2. Model Formulation

[6] Many two-dimensional models of auroral current systems have been developed in past research. In the electrostatic limit, *Doe et al.* [1995] and *Karlsson et al.* [2005] have developed one species treatments of the current closure evacuation process, which was found to be efficient in the E- and F-regions. *Noël et al.* [2000, 2005] have coupled an electrostatic solver to a flux tube model of the auroral ionosphere, and have studied the effects of impact ionization and various electron heating processes on small-scale electrodynamic structures. These studies have recently been extended by *de Boer et al.* [2010], who have also included some effects of cross-field transport of plasma. Electrodynamic models of auroral current systems are also fairly common, though the ionospheric treatment tends to be somewhat simplified. Ionospheric evacuation due to Alfvén wave currents has been simulated in a few studies focused on ionospheric feedback [*Streltsov and Lotko*, 2008] and current channel broadening [*Russell et al.*, 2010]. Three-fluid models of Alfvén wave propagation have also been developed to study effects of field-aligned currents on ionospheric heating [*Zhu et al.*, 2001].

[7] In modeling the effects of auroras on the ionosphere, the main processes of interest to the present study are frictional heating, dynamic changes in ionospheric chemistry, plasma expansion and upflow, horizontal advection of plasma, and the closure of the auroral currents. In this section we outline our new two-dimensional, electrostatic, ionospheric transport model. Alfvénic coupling is specifically neglected in the current study to facilitate the electrostatic treatment of the plasma. To self-consistently include such effects is a substantial project beyond the scope and goals of the current study.

2.1. Fluid Transport Formulation

[8] The fluid transport description of the multi-component ionospheric plasma is a variation on the 5-moment approximation, which describes the ionospheric plasma in terms of density n_s, drift velocity $\mathbf{v}_s$, and pressure p_s [*Schunk*, 1977]. These fluid equations are applied to ionospheric species relevant to the E- and F-regions, $s = O^+, NO^+, N_2^+, O_2^+, N^+$. The electrons are handled in a slightly different manner as discussed below. The 5-moment approximation is also modified to account for thermoelectric effects and thermal conduction.

[9] Densities of individual ion species s in the plasma are governed by the continuity equation.

$$\frac{\partial n_s}{\partial t} + \nabla\cdot(n_s\mathbf{v}_s) = P_s - L_s n_s \tag{1}$$

The terms on the right-hand side of the this equation encapsulate both chemical production and loss and impact ionization. In this work impact ionization is calculated using the semi-empirical method of *Rees* [1989], implemented according to the discussion in *Semeter and Kamalabadi* [2005]. Chemical reactions for the species of interest are listed in many references [*Diloy et al.*, 1996; *Huba et al.*,

2000; *Schunk*, 2000] and are not repeated here. It is worth noting, however, that the latest high-temperature reaction rates for O^+ reacting with N_2, O_2, and NO have been used [*St.-Maurice and Laneville*, 1998]. Neutral densities and temperatures needed for calculating reactions rates and collision frequencies are taken from the NRL-MSISE-00 empirical model [*Picone et al.*, 2002].

[10] The ion drift velocities $\mathbf{v}_s$ are described by the momentum equation:

$$m_s\left(\frac{\partial \mathbf{v}_s}{\partial t}+\mathbf{v}_s\cdot\nabla\mathbf{v}_s\right)=m_s\mathbf{g}-\frac{1}{n_s}\nabla p_s+q_s(\mathbf{E}+\mathbf{v}_s\times\mathbf{B})+\sum_t m_s\nu_{st}(\mathbf{v}_t-\mathbf{v}_s) \tag{2}$$

q_s is the charge of each species, $\mathbf{v}_t$ is the drift velocity of species t, and ν_{st} the collision frequencies of species s with species t (the index t is used to represent either a charged or neutral species). The partial pressure is given as $p_s = n_s k_B T_s$, where k_B is the Boltzmann constant. The pressure of individual species is governed by the energy equation presented, for example in *Schunk* [1977]. For present purposes it is convenient to rewrite this equation in terms of temperature. We also add a term to account for heat fluxes for each species.

$$\frac{\partial T_s}{\partial t}+\mathbf{v}_s\cdot\nabla T_s=-\frac{2}{3}T_s(\nabla\cdot\mathbf{v}_s)-\frac{2}{3n_sk_B}\nabla\cdot\mathbf{h}_s-\sum_t\frac{m_s\nu_{st}}{m_s+m_t}\left[2(T_s-T_t)-\frac{2}{3}\frac{m_t}{k_B}(\mathbf{v}_s-\mathbf{v}_t)^2\right]. \tag{3}$$

Strictly speaking, the heat fluxes should be accompanied by additional collision terms in the momentum equation and an additional transport equation (the 8-moment approximation [*Schunk*, 1977; *Blelly and Schunk*, 1993]), but these terms are neglected in the present version of the model. The heat fluxes are specified by a simple model of thermal conduction for the ions, and for the electrons, both thermoelectric effects and thermal conduction are considered.

$$\mathbf{h}_s=-\lambda_s\nabla T_s \tag{4}$$

$$\mathbf{h}_e=-\lambda_e\nabla T_e-\beta_e\mathbf{J} \tag{5}$$

Here, λ_s is the thermal conductivity for ion species s [*Banks and Kockarts*, 1973], and λ_e and β_e are the electron thermal conductivity and thermoelectric coefficients, respectively [*Schunk and Nagy*, 1978]. As a further simplification, the heat flux is assumed to be primarily along the magnetic fields lines in the development that follows.

2.2. Electrostatic Approximation

[11] For a coupled description of transport and electrodynamics in auroras, the fluid equations presented above must be supplemented by Maxwell's equations. However, the issue of finding the ionospheric electric field that results from a given magnetospheric boundary condition may be treated, to some degree of accuracy, as an electrostatic problem. The details of this approximation have been covered by several authors [e.g., *St.-Maurice et al.*, 1996, and references therein], and the net effect is that the displacement current and electromagnetic induction may be neglected in situations where wave dynamics are not important or have negligible effects. This approximation precludes modeling of Alfvén waves and related inductive M-I coupling effects as discussed, for example in *Lotko* [2004]. Our focus in the following sections on slowly varying current systems supports this use of the electrostatic approximation.

[12] Quasi-neutrality holds very strongly in the plasma so it may be assumed that $n_e \approx \sum_{s\neq e} n_s$. In addition, a steady-state momentum balance holds under certain conditions (discussed below), which allows the velocities to be expressed in a simple way as a function of the electric field. These facts mean that the steady state current continuity equation, given by

$$\nabla\cdot\mathbf{J}=\nabla\cdot\left(\sum_s n_sq_s\mathbf{v}_s\right)=0, \tag{6}$$

may be used to directly solve for electric potential as detailed below.

2.3. Momentum Balance Approximation and Ohm's Law

[13] A steady state momentum balance assumption yields a direct solution for drifts in terms of electric fields, pressures, and neutral winds. If the left hand side of equation (2) is neglected, along with gravitational forces, then the drifts are proportional to the force per unit charge:

$$\mathbf{v}_{s\perp}=\boldsymbol{\mu}_{s\perp}\cdot\left(\mathbf{E}_\perp-\frac{1}{n_sq_s}\nabla_\perp p_s+\frac{m_s\nu_s}{q_s}\mathbf{v}_{n\perp}\right) \tag{7}$$

$$\mathbf{v}_{e\parallel}=\mu_{e0}\left(\mathbf{E}_\parallel-\frac{1}{n_eq_e}\nabla_\parallel p_e\right) \tag{8}$$

$\mathbf{v}_n$ is the neutral wind velocity, and the mobilities are defined in Cartesian coordinates with $\mathbf{B}$ in the z-direction by:

$$\boldsymbol{\mu}_{s\perp}\equiv\frac{q_s}{m_s\nu_s}\begin{bmatrix}\frac{\nu_s^2}{\nu_s^2+\Omega_s^2} & \frac{\nu_s\Omega_s}{\nu_s^2+\Omega_s^2}\\ -\frac{\nu_s\Omega_s}{\nu_s^2+\Omega_s^2} & \frac{\nu_s^2}{\nu_s^2+\Omega_s^2}\end{bmatrix}=\begin{bmatrix}\mu_{sP} & -\mu_{sH}\\ \mu_{sH} & \mu_{sP}\end{bmatrix} \tag{9}$$

$$\mu_{e0}\equiv\frac{q_e}{m_e\nu_e'} \tag{10}$$

The cyclotron frequency is $\Omega_s \equiv q_sB_z/m_s$, and the total collision frequency is represented by ν_s. For the mobilities μ_{sP} and μ_{sH}, the total collision frequency is calculated as a sum over ion-neutral collisions, which are dominant in regions where perpendicular transport is important.

$$\nu_s=\sum_n\nu_{sn} \tag{11}$$

Both electron-neutral and electron-ion collisions are used in computing the parallel mobility of the electrons, which dominates the parallel conductivity. The Coulomb collisions

are necessary since the field-aligned currents carried by electrons flow at high altitudes.

$$\nu_e' = \sum_n \nu_{en} + \sum_j \nu_{ej} \tag{12}$$

In this equation the quantity ν_{ej} refers to collisions of electrons with charged species j. As a final note, neutral and ion drifts are neglected in the computation of the parallel electron drift, which is assumed to be much larger than any other flows.

[14] The steady-state momentum balance (equations (7) and (8)) is justified in the sense that the principle charge carriers, electrons in the field-aligned direction and ions perpendicular to **B**, attain a steady-state quickly. The ions drift perpendicular to the field in a steady state for time scales $\tau \gg 2\pi\Omega_s^{-1}$. Electrons are in a steady-state in field-parallel direction on time-scales much longer than the electron collision time (probably 10^{-2} s or less) [e.g., *St.-Maurice et al.*, 1996]. Because of these considerations, we may multiply the momentum balance by $n_s q_s$ and sum over species to obtain an Ohm's law.

$$\mathbf{J}_\perp = \boldsymbol{\sigma}_\perp \cdot \mathbf{E}_\perp - \sum_s \boldsymbol{\mu}_{s\perp} \cdot \nabla_\perp p_s + \sum_s n_s m_s \nu_s \boldsymbol{\mu}_{s\perp} \cdot \mathbf{v}_{n\perp} \tag{13}$$

$$\mathbf{J}_\parallel = \sigma_0 \mathbf{E}_\parallel - \mu_{e0} \nabla_\parallel p_e \tag{14}$$

with the conductivities defined by:

$$\boldsymbol{\sigma}_\perp \equiv \sum_s n_s q_s \boldsymbol{\mu}_{s\perp} = \begin{bmatrix} \sigma_P & -\sigma_H \\ \sigma_H & \sigma_P \end{bmatrix} \tag{15}$$

$$\sigma_0 \approx n_e q_e \mu_{e0} \tag{16}$$

In doing so we note that the ion drift in the parallel direction is not generally in a steady-state but that the ion terms are, in any case, irrelevant contributors to the parallel conductivity. This is due to the large parallel electron mobility, which causes the electron terms to dominate the summation over charged species needed to compute current density.

2.4. Ambipolar Field Separation

[15] In this work the ambipolar part of the electric field is separated out when solving for potential, and then added back into the momentum equation when the forces are accumulated. This is done (for now) to avoid an equation for electric potential with source terms involving second derivatives of numerically determined quantities. The specific approach is to split the electric field into two parts, the ambipolar field $\mathbf{E}_a$ which is present even in the absence of magnetospheric forcing and neutral winds, and the response field $\mathbf{E}_r$ which results from magnetospherically imposed currents and/or neutral winds. The familiar expression for the parallel component of the ambipolar field is obtained by zeroing out **J** in equation (14).

$$\mathbf{E}_{a\parallel} \approx \sigma_0^{-1} \mu_{e0} \nabla_\parallel p_e = \frac{1}{n_e q_e} \nabla_\parallel p_e \tag{17}$$

At present we neglect contributions of perpendicular pressure gradients to current, which are unlikely to be important compared to applied electric fields used to drive the model in this study. Ohm's law with $\mathbf{E} = \mathbf{E}_r + \mathbf{E}_a$ becomes an equation in the disturbance quantities only.

$$\mathbf{J}_\perp = \boldsymbol{\sigma}_\perp \cdot \mathbf{E}_{r\perp} + \sum_s n_s m_s \nu_s \boldsymbol{\mu}_{s\perp} \cdot \mathbf{v}_{n\perp} \tag{18}$$

$$\mathbf{J}_\parallel = \sigma_0 \mathbf{E}_{r\parallel} \tag{19}$$

Invoking the electrostatic assumption $\mathbf{E}_r = -\nabla\Phi$ gives an equation that can be solved directly for electric potential.

$$\nabla_\perp \cdot (\boldsymbol{\sigma}_\perp \cdot \nabla_\perp \Phi) + \nabla_\parallel \cdot \left(\sigma_0 \nabla_\parallel \Phi\right) = \nabla_\perp \cdot \left(\sum_s n_s m_s \nu_s \boldsymbol{\mu}_{s\perp} \cdot \mathbf{v}_{n\perp} \right) \tag{20}$$

Note that this problem becomes homogeneous if neutral winds are neglected, while inclusion of the inhomogeneous terms allows for modeling of neutral drag effects on current generation.

[16] The general simulation of ionospheric dynamics is a simultaneous solution of equations (20), (1), (2), and (3) for the unknowns Φ, n_s, $\mathbf{v}_s$, and T_s. As outlined above, momentum balance is assumed in the computation of Φ at any particular instant. The evolution of potential on longer times scales is captured by evaluating the steady state equation equation (20) at each time step as the fluid variables (densities, etc. hence conductivities) are updated.

2.5. Two-Dimensional Form of Model

[17] In the simulations in this paper, a two-dimensional form of the equations listed above is used. The scenario that we wish to model is an auroral current system that is elongated in the longitudinal dimension, compared to its latitudinal size. Hence, variations in longitude are neglected, rendering the problem two-dimensional. Finally, if the upper altitude of interest is not too high, then the magnetic field lines are roughly parallel, the magnitude of the magnetic field is roughly constant, and we may also employ a Cartesian form for the spatial derivatives.

[18] The Cartesian form of the model equations results from straightforward manipulation of the general equations outlined in the previous section. For notational simplicity the following symbols are defined:

$$\mu_P' \equiv \sum_s n_s m_s \nu_s \mu_{sP} \qquad \mu_H' \equiv \sum_s n_s m_s \nu_s \mu_{sH} \tag{21}$$

Using these definitions and zeroing out the y-derivatives gives the following elliptic equation for potential.

$$\sigma_P \frac{\partial^2 \Phi}{\partial x^2} + \sigma_0 \frac{\partial^2 \Phi}{\partial z^2} + \frac{\partial \sigma_P}{\partial x}\frac{\partial \Phi}{\partial x} + \frac{\partial \sigma_0}{\partial z}\frac{\partial \Phi}{\partial z} = \frac{\partial}{\partial x}(\mu_P' v_{nx}) - \frac{\partial}{\partial x}\left(\mu_H' v_{ny}\right) \tag{22}$$

In this equation and the following development, z is along the geomagnetic field and x is the north-south direction (assumed to be positive north, though this designation does not matter for the development at hand). The perpendicular velocities may be directly obtained from equation (7) once the electric potential is known.

[19] Fully time-dependent equations are solved for the parallel velocity, density, and temperatures. These fluid equations are, at least partially, implemented in conservative form for numerical reasons.

$$\frac{\partial n_s}{\partial t}+\frac{\partial}{\partial x}(n_s v_{sx})+\frac{\partial}{\partial z}(n_s v_{sz})=P_s-L_s n_s \tag{23}$$

$$\frac{\partial v_{sz}}{\partial t}+\frac{\partial}{\partial x}(v_{sz}v_{sx})+\frac{\partial}{\partial z}\left(\frac{1}{2}v_{sz}v_{sz}\right)=\frac{\partial v_{sx}}{\partial x}v_{sz}-g-\frac{1}{m_s n_s}\frac{\partial p_s}{\partial z}+\frac{q_s}{m_s}E_z+\sum\nolimits_t \nu_{st}(v_{tz}-v_{sz}) \tag{24}$$

Equations of this form are solved for each positive ion species. For the electrons the density and velocities are found from quasi-neutrality and the definition of current density.

$$n_e \approx \sum_{s\neq e} n_s \tag{25}$$

$$\mathbf{v}_e=-\frac{1}{n_e q_e}\left(\sum_{s\neq e} n_s q_s \mathbf{v}_s-\mathbf{J}\right). \tag{26}$$

[20] The temperature equations for the ion species differ slightly from the electrons. For ions, the temperature equation is:

$$\begin{aligned}\frac{\partial T_s}{\partial t}&+\frac{\partial}{\partial x}(T_s v_{sx})+\frac{\partial}{\partial z}(T_s v_{sz})\\ &=\frac{1}{3}T_s\left(\frac{\partial v_{sx}}{\partial x}+\frac{\partial v_{sz}}{\partial z}\right)+\frac{2}{3n_s k_B}\frac{\partial \lambda_s}{\partial z}\frac{\partial T_s}{\partial z}+\frac{2\lambda_s}{3n_s k_B}\frac{\partial^2 T_s}{\partial z^2}\\ &\quad-\sum_t \frac{m_s\nu_{st}}{m_s+m_t}\left[2(T_s-T_t)-\frac{2}{3}\frac{m_t}{k_B}\left\{(v_{sx}-v_{tx})^2+(v_{sy}-v_{ty})^2\right.\right.\\ &\quad\left.\left.+(v_{sz}-v_{tz})^2\right\}\right].\end{aligned} \tag{27}$$

For electrons the heat flux contains a current term, i.e., equation (5), which is calculated from the formulas presented for the thermoelectric coefficient in *Schunk and Nagy* [1978]. The electron temperature equation in 2-D form is given by:

$$\begin{aligned}\frac{\partial T_e}{\partial t}&+\frac{\partial}{\partial x}(T_e v_{ex})+\frac{\partial}{\partial z}(T_e v_{ez})\\ &=\frac{1}{3}T_e\left(\frac{\partial v_{ex}}{\partial x}+\frac{\partial v_{ez}}{\partial z}\right)+\frac{2}{3n_e k_B}\left(\frac{\partial \lambda_e}{\partial z}+\frac{5}{2}\frac{k_B J_z}{|q_e|}\right)\frac{\partial T_e}{\partial z}\\ &\quad+\frac{2\lambda_e}{3n_e k_B}\frac{\partial^2 T_e}{\partial z^2}-\sum_t \frac{m_s\nu_{et}}{m_e+m_t}\left[2(T_e-T_t)-\frac{2}{3}\frac{m_t}{k_B}\left\{(v_{ex}-v_{tx})^2\right.\right.\\ &\quad\left.\left.+(v_{ey}-v_{ty})^2+(v_{ez}-v_{tz})^2\right\}\right].\end{aligned} \tag{28}$$

[21] Equations (22)–(28) are *exactly* the equations implemented in the current iteration of the model.

2.6. Numerical Methods

[22] Equation (22) for electric potential is solved through a finite difference technique, which generates a sparse system of linear equations that can be solved using standard numerical linear algebra routines (both LU factorization and iterative methods have been tried). The fluid equations are solved through a time-step splitting scheme that is used to separate the pure advective parts of the equations (the left-hand sides of (23), (24), (27)) from the source and diffusion terms (the right-hand sides). The advective portion is solved using an explicit finite volume technique. Different specifications of cell wall fluxes are implemented in the current iteration of the model (donor cell flux, minmod limited flux, or monotonized central difference limited flux (MC)) but the best results have been achieved with the MC limiter, which preserves sharp gradients at the current system edges better than the other methods. For the continuity and momentum equations, once the advective portion has been computed we are left with a pure source/loss differential equation. This equation is solved analytically by using previous time step values to calculate source terms and loss rates. The energy equations sans advective terms become diffusion problems which are solved with an implicit finite difference technique. For these diffusion problems, either backward Euler or 2nd order, trapezoidal backward difference methods may be used for time integration and centered differences are used for the spatial derivatives.

3. Simulations of Slowly Varying Current Systems

[23] To illustrate the basic features of plasma redistribution in auroras, the model is run with zero background winds and an applied topside potential corresponding to an electric field of Gaussian shape with a peak value of 110 mV/m. This electric field is applied at 1000 km altitude and is shown in Figure 1a along with the field aligned current at the beginning of the model run. The topside potential is held constant for the 10 min duration of the model run, and the field aligned current evolves as the conductivities change. These conditions are deliberately chosen to be representative of a very strong frictional heating event, so as to clearly exhibit the relevant physical processes. The initial ionospheric conditions are (simulated) equilibrium profiles in the z-direction and uniform in the x-direction, shown in Figures 1b–1d. A weak flux ($\sim$0.1 mW/m^2) of 3 keV electrons has been applied to model diffuse precipitation and to produce a background Pedersen conductivity of $\sim$1.5 Ω. The initial plasma density shown in Figure 1b is representative of the nighttime high-latitude conditions observed in *Zettergren et al.* [2010].

[24] Figure 2 shows a snapshot of the ionosphere 5 min after the electric field is applied to the initially uniform (in the x-direction) plasma. Figures 2a–2f show, respectively: parallel current density, perpendicular current density, plasma density, ratio of O^+ density to total plasma density, average ion temperature, and average parallel ion drift velocity. The temperature and drift is a species average defined by:

$$T_i\equiv\frac{\sum_{s\neq e} n_s T_s}{\sum_{s\neq e} n_s} \qquad v_{iz}\equiv\frac{\sum_{s\neq e} n_s v_{sz}}{\sum_{s\neq e} n_s} \tag{29}$$

Quite drastic modifications to the ionospheric plasma result from the current system. First, Figure 2a shows that the initially symmetric up-down current pair has been distorted due

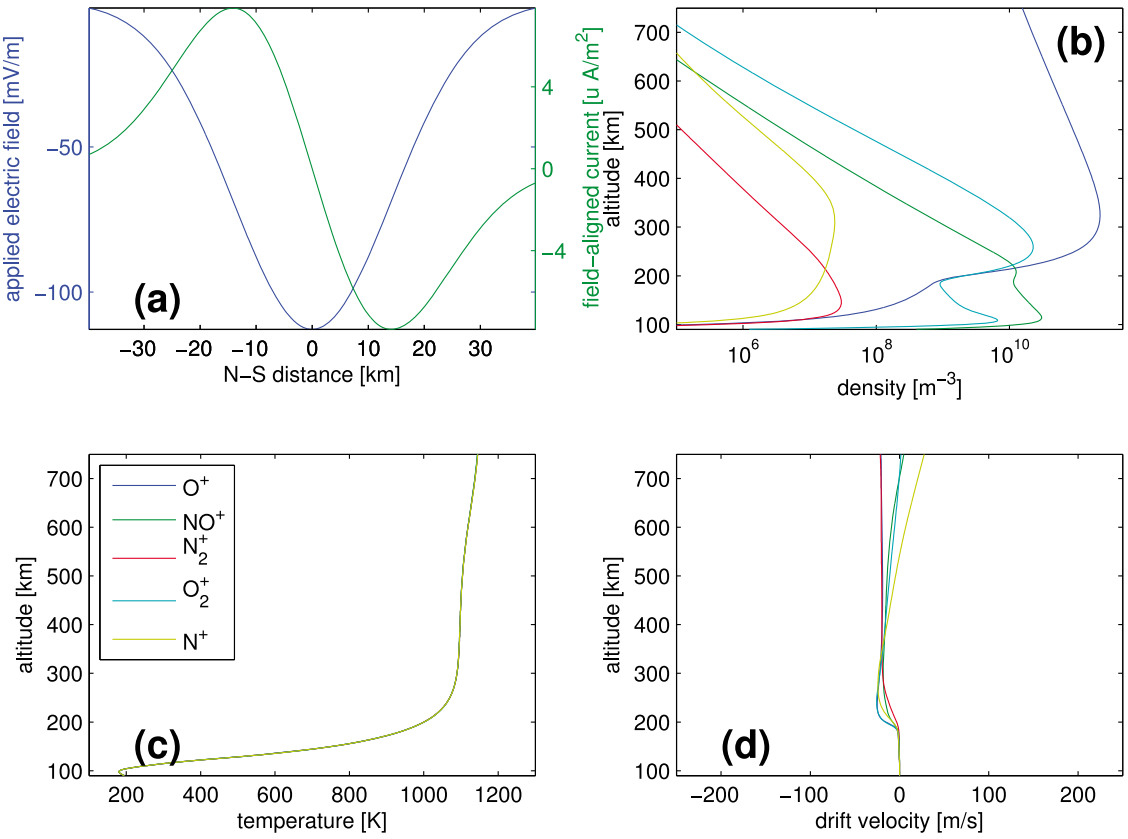

Figure 1. Initial and boundary conditions for the mesoscale current system simulation. (a) Electric field and initial field-aligned current. (b) Ion densities. (c) Ion temperatures (all are approximately equal to T_n since no frictional heating has been applied to generate these initial conditions). (d) Ion drift velocities.

to broadening of the downward current region. This broadening is a result of the depletion of the E-region plasma (Figure 2c), which forces the current channel to broaden in order to access more charge carriers. Due to the depletion of the E-region, the perpendicular current begins to close a small amount through the F-region ionosphere ($-20 \leq x \leq 20$ km, $200 \leq z \leq 300$ km), as shown in Figure 2b. The E-region depletion process, and reconfiguration of the parallel and perpendicular currents occur very quickly, on time scales of 5–30 s. The extreme ion heating in the F-region (Figure 2e) occurs on similar time scales and begins converting the F-region plasma to molecular ions (mostly NO^+). This process becomes apparent within 120–150 s. The moleculars recombine more quickly than O^+ and so an F-region depletion forms due to the enhanced recombination and the current closure depletion (Figure 2f). Finally the topside heating, which occurs in about 60 s, generates rather intense ion upflows (Figure 2f). These upflows initially increase the density around 500 km altitude, but then begin to move the plasma from this region into the far topside ionosphere (altitudes >600 km).

[25] The simulation presented in Figure 2 ignores the possibility of intense electron precipitation in the upward current region which would be common, for example, in a discrete auroral arc. On the surface it is not clear whether the presence of suprathermal electrons in the upward current region (UCR) would affect the behavior of the current system greatly. Impact ionization and conductivity enhancements at the arc's edge should factor into the solution of equation (22) and may alter fields and heating nearby. The effects of this process are evaluated by running the simulation with a field-aligned current top boundary conditions for two cases: a thermal current system with only very weak background precipitation (0.1 mW/m^2), and a discrete arc current system containing a strong flux of suprathermal electrons in the UCR in addition to the background flux. Both simulations have identical top boundary conditions on field-aligned current, which is used to insure that the applied precipitation is entirely restricted to the UCR. The discrete arc suprathermal flux was chosen to be representative of an inverted-V type precipitating population. Specifically, the peak energy flux is 5 mW/m^2 at a characteristic energy of 10 keV and is attenuated in both energy flux and characteristic energy toward the edges of the UCR in proportion to the applied top boundary current. The energy shape of the precipitating electrons is Maxwellian.

[26] A comparison of the thermal current system and the discrete arc is shown in Figure 3, in terms of FAC and electron density after 300 s of simulation time. Figures 3a and 3c show the thermal current system, while Figures 3b and 3d show the discrete arc. Away from the UCR/DCR boundary the parallel currents and electron densities in the DCR are very similar. Both E- and F-region depletions are manifest in the results. The E-regions of the UCR are quite

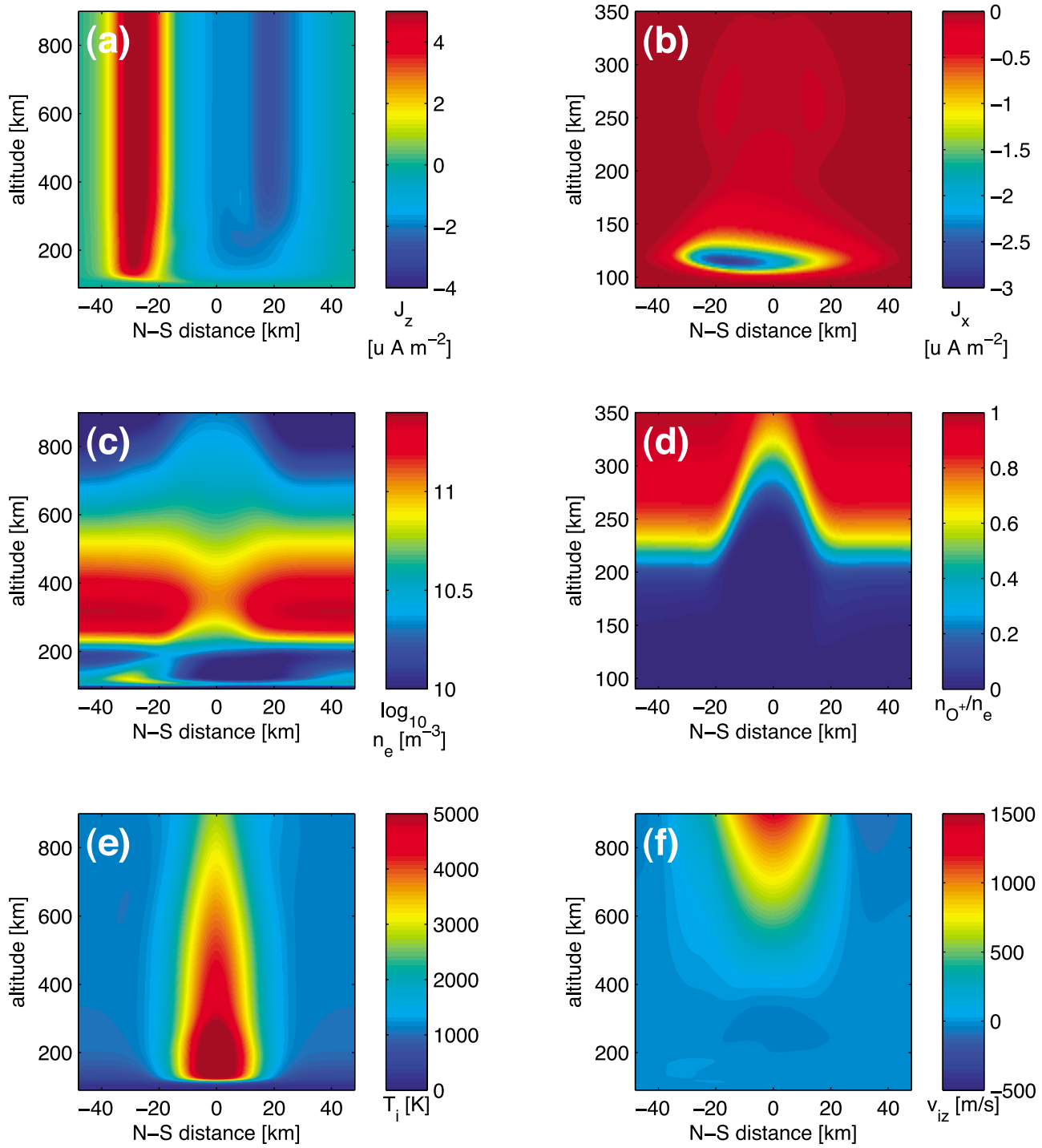

Figure 2. Two-dimensional model results for inputs of Figure 1 after 300 s. (a) Field-aligned current. (b) Field-perpendicular current. (c) Electron density. (d) Ratio of O^+ density to total plasma density. (e) Average ion temperature. (f) Average ion drift velocity.

different, obviously, due to the impact ionization in the discrete arc. The region right at the UCR/DCR boundary ($x \approx 0$) also displays some very interesting differences. In particular the FAC in the discrete arc simulation (Figures 3b and 3d) reconfigures due to enhanced conductivity near the UCR edge. This causes additional plasma redistribution not present in the thermal simulation. However, it is not clear how physical this behavior is, since the top boundary conditions (current and electron flux) are driven in an *ad hoc* manner, when, in fact they are likely to be related somehow. In spite of the differences shown in Figure 3, the bulk of the DCR response is similar in both cases. Thus, we neglect discrete arc precipitation effects in the remainder of the present study, and, in doing so, restrict our attention to the DCR away from the UCR boundary.

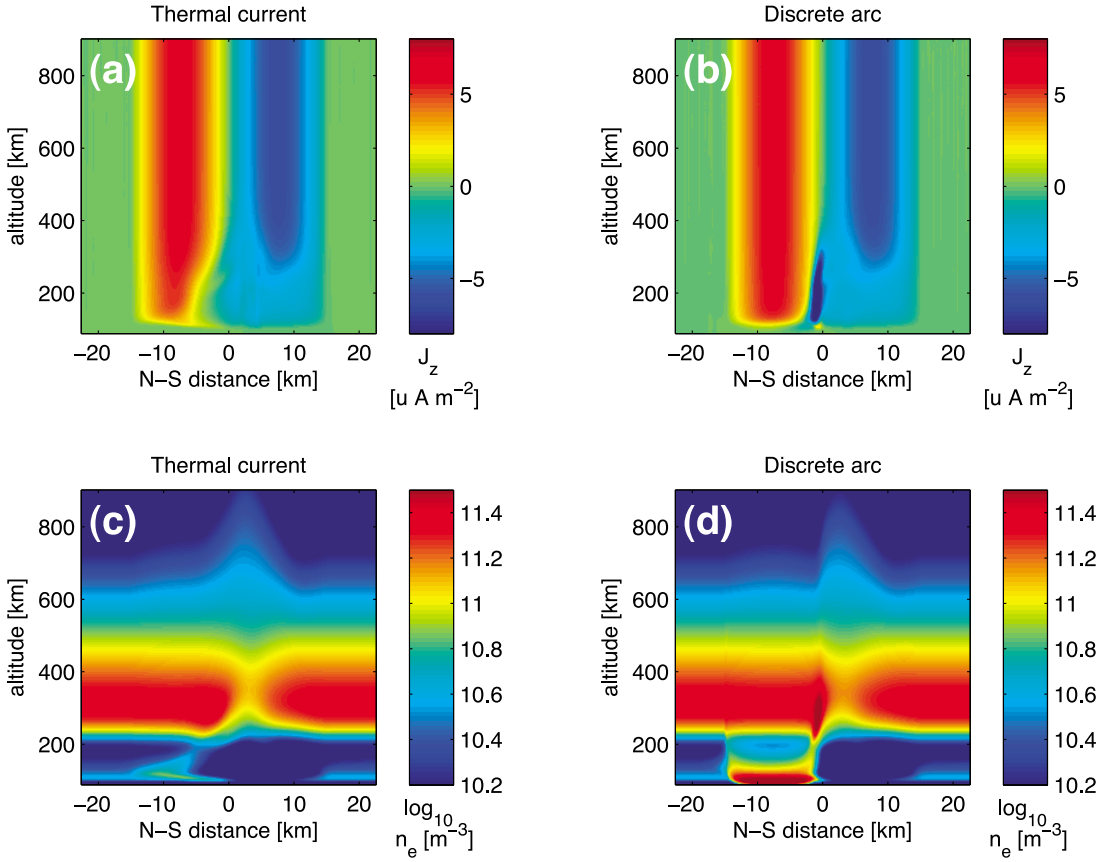

Figure 3. Comparison of ionospheric plasma density in a 300 s simulation with field-aligned current boundary condition. (a and c) Thermal current system field-aligned current and electron density, respectively. (b and d) Discrete arc field-aligned current and electron density, respectively.

3.1. Depletion Processes: Current Closure Versus Recombination

[27] A comparison of plasma density profiles modeled with and without frictional heating reveals the relative contributions of these processes in the E- and F-regions. In model runs without the frictional heating we set $T_s = T_n$ (neutral temperature) in lieu of solving the energy equations. The collision terms in the momentum equation are retained so that the ions/currents flow normally. Such an *ad hoc* exclusion of the energy equation is, of course, unrealistic, but is useful to demonstrate the effects of frictional heating. Figure 4 shows density profiles computed by the code with all physics present, and density modeled with frictional heating switched off. These profiles are extracted from the *x*-location where the F-region plasma density is a minimum (roughly the center of the downward current region). The simulation without friction includes only the current closure depletion, and allows determination of the efficiency of each depletion process for various ionospheric altitudes. Figure 4a shows this analysis for a mesoscale current system having background conductivity of $\sim$1 Ω. The solid and dashed lines, showing density with and without frictional heating, clearly demonstrate that the F-region peak depletion is due to the frictional heating, subsequent conversion of the plasma to molecular ions, and then recombination. It is furthermore apparent that the E-region and lower F-region depletions are entirely due to current closure.

[28] The depletion processes are dependent, to a degree, on the size of the current system. Figure 4b shows profiles modeled for a current system one quarter the width of that shown in Figure 4a. As before, these profiles are extracted from the *x*-location where the F-region plasma density is a minimum. The top boundary perpendicular electric field is kept constant and the initial conductivity is $\sim$1 Ω, so the perpendicular current is initially also the same. However, the width of the upward and downward current channels is decreased by a factor of 4, so that the initial topside current density has a maximum of 18 μA/m^2, in contrast to the mesoscale initial current of 4.5 μA/m^2. The increased current density makes the current closure depletion process more efficient and results in a much lower E-region density in both simulations in Figure 4b. The simulation without frictional heating also shows that decreasing the scale size makes this process more efficient at evacuating the F-region peak, although it is still not as efficient as the frictional heating (which is not affected by the different current system size).

[29] It is clear that the recombination process should depend only on the applied electric field and resulting frictional heating and not the size of the current system. The effective recombination coefficient depends on the composition of the plasma, which is controlled by temperature-sensitive reaction rates. The physical reason for the dependence of current closure depletion on scale size can be understood through the

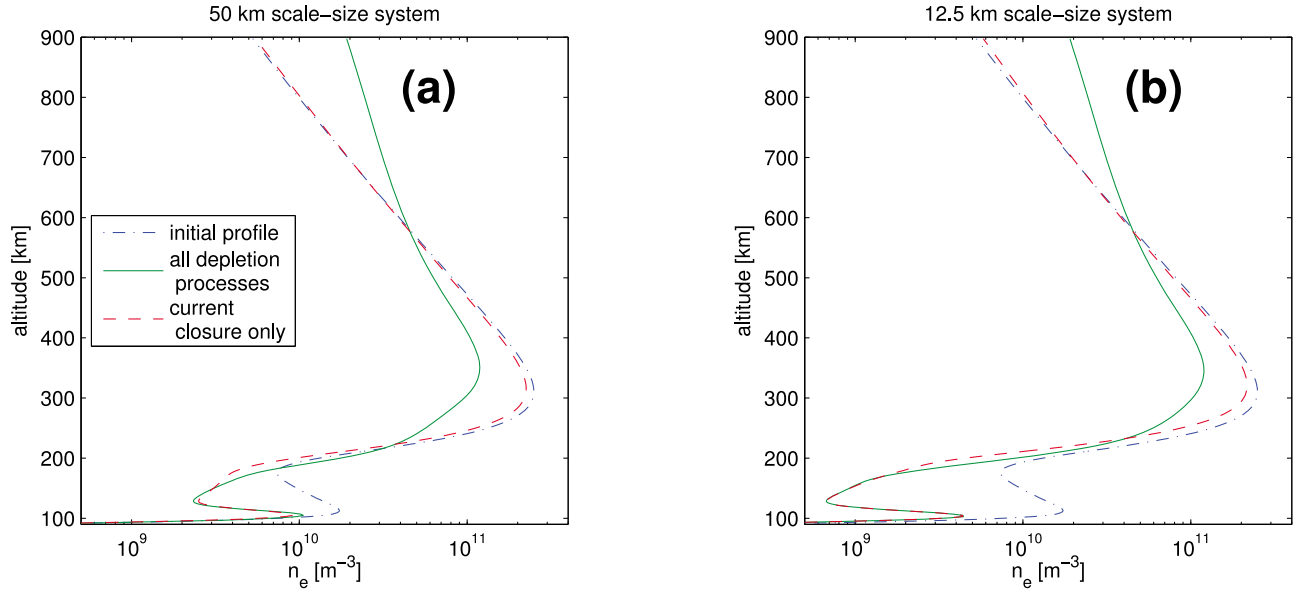

Figure 4. Comparison of depletion mechanisms. (a) Mesoscale current system. (b) Smaller scale system.

electron continuity equation (equation (1) with $s = e$). The equation can be cast in terms of current densities by invoking equation (26) for the parallel component of the electron drift, assuming singly ionized ionospheric constituents with no negative ions other than e^-, and noting that the perpendicular electron drift is, to a high degree of accuracy, $\mathbf{E} \times \mathbf{B}/B^2$ in the E-region. Finally the perpendicular drift is taken to be incompressible, so that $\nabla_\perp \cdot \mathbf{v}_{e\perp} = 0$. These assumptions yield [e.g., *Doe et al.*, 1993, 1995]:

$$\frac{\partial n_e}{\partial t} = P_e - L_e n_e - \frac{\partial}{\partial z}\left(\sum_s n_s v_{sz}\right) - \frac{1}{q_e}\frac{\partial J_z}{\partial z} - \nabla_\perp n_e \cdot \mathbf{v}_{e\perp} \quad (30)$$

The first two terms of this equation are chemical sources and loss, the third term represents the ambipolar part of the field-aligned motion, the fourth term is current closure loss/gain, and the final term represents advection of density gradients. By invoking current continuity, the current term in this equation can be rewritten as:

$$-\frac{1}{q_e}\frac{\partial J_z}{\partial z} = \frac{1}{q_e}\nabla_\perp \cdot \mathbf{J}_\perp = -\frac{1}{e}\nabla_\perp \cdot \mathbf{J}_\perp, \quad (31)$$

where e is the elementary charge. This relation shows that the density decreases at regions where the perpendicular current originates. The current closure loss is therefore clearly dependent on the perpendicular scale size of the system. The factor of four decrease in current system size should, therefore, deplete the plasma more, as indicated by the model results.

4. Systematic Analysis of Ionospheric Response to Steady Forcing

[30] A large set of simulations is presented in this section to quantitatively evaluate the basic features illustrated in the model run of Figure 2. Each simulation represents the step response of the ionosphere to a constant electric field between 0 and 220 mV/m. By varying the applied electric field, the model is able to characterize the ionospheric response to a wide range of heating situations. As before, we neglect all precipitation except for a weak background flux, which sets up a poorly conducting background E-region (~1–2 Ω). Neutral winds are neglected in these model runs. Figure 5 shows the response of various F-region and topside ionospheric parameters vs. electric field strength and time after field is applied.

[31] Figures 5a and 5b show O^+ fluxes at 750 km altitude and molecular ion fluxes at 375 km altitude. Both constituent upflows display significant transients that are dependent on the applied electric field. Generally, stronger fields (and heating) result in shorter response times at both altitudes in both constituents. For commonly observed arc electric fields (say 50–100 mV/m), the upflow processes take a few minutes to fully initiate. Peak fluxes in these cases tend to occur about 3–4 minutes after initiation of electric fields and heating. At the higher altitudes almost all of the upflow is O^+, while near the F-region peak the upflows, at least for strong electric field forcing, are molecular (this result is not directly shown in the figure).

[32] Plasma loss processes in the F-region (300 km) and topside (500 km) are summarized in Figures 5c and 5d. Again, the time constants of the response decrease with increasing electric field. For electric field values of greatest interest (50–100 mV/m) roughly 2–5 mins are required for a relative depletion of 50% to form in the F-region. In the topside the depletions are smaller and take longer to initiate since they are caused by slower transport processes. Topside densities at 500 km initially increase slightly after the field is applied due to the transport of plasma from the F-region peak. This effect subsides at longer times since the plasma transport continues upward into the far topside.

[33] Figure 5e shows the crossover altitude for molecular plasma to atomic ion plasma, defined as the altitude where the plasma is equal parts molecular and atomic [*Zettergren et al.*, 2011]. Typically this parameter has nighttime

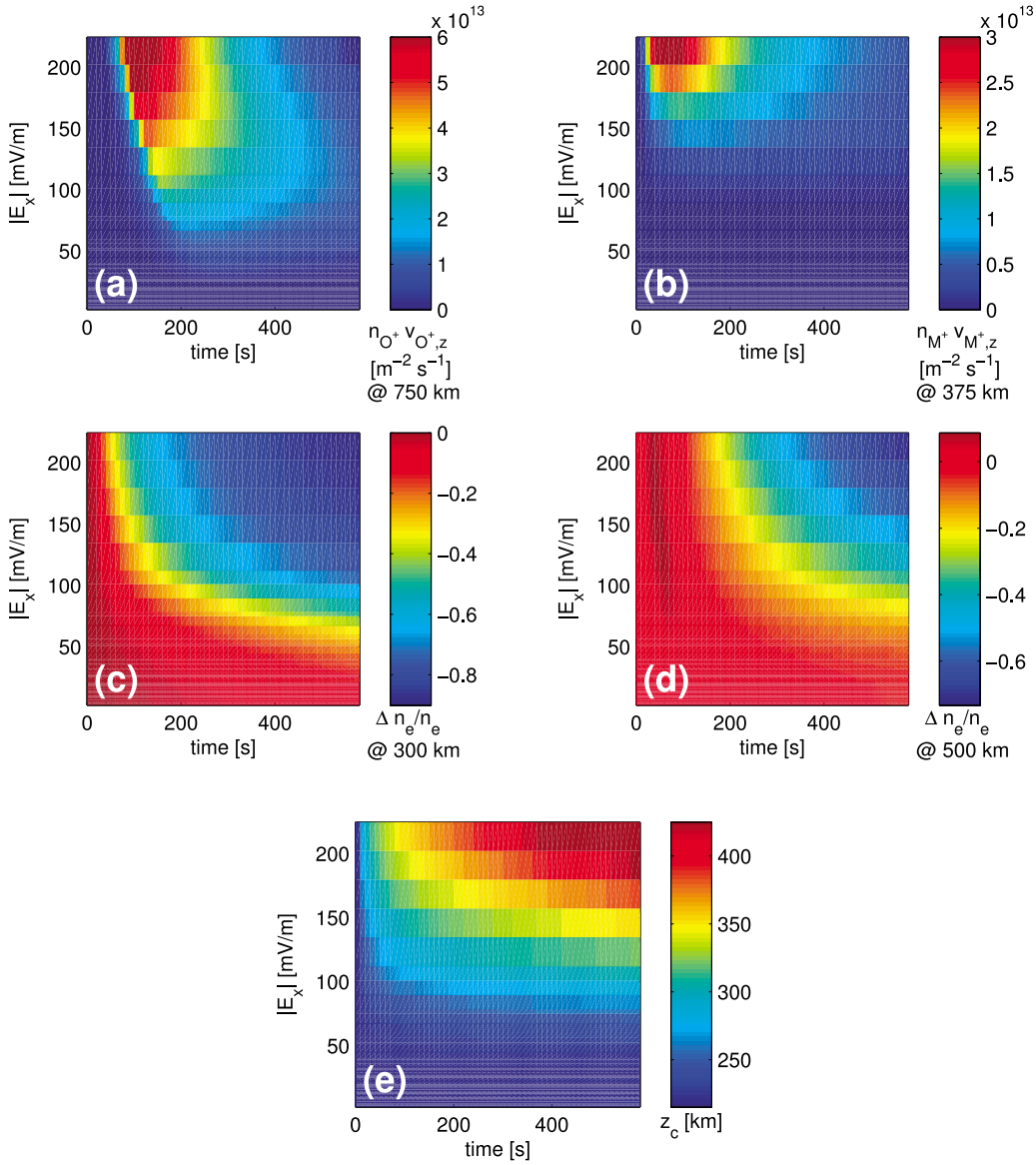

Figure 5. Simulation results demonstrating plasma parameter dependence on applied electric field magnitude and time of exposure. (a) O^+ fluxes at 750 km. (b) Molecular ion fluxes at 375 km. (c) Relative variations in F-region density at 300 km. (d) Relative variations in topside density at 500 km. (e) Crossover altitude (location where plasma is equal parts atomic and molecular ions).

undisturbed values of ~220 km (see unperturbed region of Figure 2d). Time constants are typical of the other F-region processes discussed above and are, likewise, electric field dependent. Typical disturbance auroral electric field values raise the crossover altitude to near the F-region peak (~250–300 km), while more extreme values (>110 mV/m) are capable of generating molecular ions in the topside. This process may be responsible for producing a source population of molecular ions for higher altitude energization processes.

[34] It has been suggested that type-1 upflows may be self-limiting since the heating also causes enhanced recombination [*Zettergren et al.*, 2011]. The simulations demonstrate that this is not the case for the broad range of electric fields considered - more heating means more upflow irrespective of the attendant recombination. The physical reason is that the upflows seen, e.g., at 750 km (Figure 5a) are initiated from the F-region and topside ionosphere [e.g., *Zettergren et al.*, 2007, Figure 1] and occur faster than the recombination, which starts below the F-region peak and spreads upward. By the time the moleculars are generated at the F-region peak (Figure 5e) the upflow has already worked its way into the far topside.

[35] The parameters discussed above are dependent on the electric field value regardless of the scale size of the current system. However, as indicated in equations (30) and (31) the E-region current closure depletion should depend strongly on the scale size of the system for a given applied electric field. Figure 6 presents a set of simulations with fixed **E** but with each simulation having a different perpendicular scale size ranging from 2–20 km. For purposes of this discussion

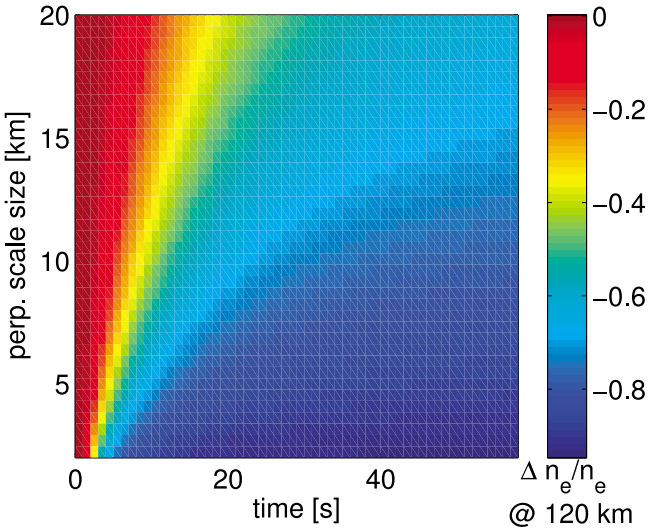

Figure 6. Simulation results demonstrating E-region density dependence on current system scale size.

we formally define the scale size Δx according to the topside potential boundary condition which is of the form:

$$\Phi(z = 1000[\text{km}], x) = \Phi_0 \text{erf}\left(\frac{x}{\Delta x}\right) \tag{32}$$

so that the applied electric field has a Gaussian shape with scale size Δx. Background conductivity for these simulations was ~2 Ω. The relative change in plasma density at 120 km altitude shown in Figure 6 has a very short time constant which depends strongly on scale size. The large scale systems (15–20 km) take about 45 s to produce a 50% depletion, while the smaller scales do so in less than 5 s. For a steady applied electric field, the depletions ultimately exceed 90%, for smaller scales as quickly as 20–30 s.

5. Influence of Neutral Dynamics

[36] Neutral atmospheric disturbances can affect ion chemistry (by changing concentrations of reactants), electrodynamics (through the dynamo effect), and frictional heating (by altering differential ion-neutral drift). This section explores the ionospheric response to applied current systems under conditions of disturbed neutral atmospheric densities and winds. The neutral atmosphere is not self-consistently included in the current version of the model, but all of the relevant ion-neutral coupling terms are included in the solution of the electrostatic and fluid equations, so we may impose neutral atmosphere density changes and winds to simulate their ionospheric effects.

[37] Variations in the O/N_2 ratios are extremely commonplace at high latitudes [e.g., *Strickland et al.*, 1999]. Qualitatively, the effects of increasing or decreasing N_2 concentrations, for example, are easy to describe. The primary chemical pathway for O^+ to be converted into NO^+ is through a reaction with N_2 [*St.-Maurice and Laneville*, 1998]. Increasing the density of N_2 will obviously speed up the generation of moleculars, while decreasing it will slow it down. Figure 7 shows a systematic analysis of these effects resulting from a sequence of model runs. Three different atmospheres corresponding to variations of the standard MSIS results were chosen, and for each atmosphere the model was run for many different values of electric field ranging from 20–130 mV/m (the fields are applied for 5 mins. in each simulation). The results are summarized in Figure 7 in terms of crossover altitude vs. electric field for the three different atmospheres. Doubling or halving the density of molecular nitrogen has a significant effect on how the ionosphere responds to the applied auroral electric field, effectively shifting up or down the crossover altitude by 10–25 km.

[38] Vertical neutral winds (v_{nz}) will also affect the composition and distribution of plasma. Simulations suggest that winds of 10–30 m/s along the field line can slightly raise the crossover altitude, but the effects are not large enough (compared to other processes of interest) to show here or to warrant further discussion. Larger vertical winds (50–100 m/s) can begin to have substantial effects, but such winds appear to be rare.

[39] Extended periods of ion flow can transfer enough momentum to the neutral atmosphere to generate large horizontal winds. Since the time constant for this process is altitude dependent (the plasma density and collision frequency depend on altitude), it is possible that the horizontal winds could have a strong altitude dependence. Examination of the ion energy equation (equation (3)) indicates that this will cause vertical structure in frictional heating and ion temperature. This possibility appears to have received little attention in the literature but is important since many of the methods developed to extract ion composition from incoherent scatter radar data rely on being able to accurately model the ion temperature profile. In particular the techniques developed by *Blelly et al.* [2010]; *Zettergren et al.* [2011] assume that the horizontal neutral wind is constant with altitude through the F-region. Figure 8 shows structured winds based on simulations by *St.-Maurice and Schunk* [1981] used to drive the ionospheric model developed in this work. Their simulated horizontal neutral wind profiles have been taken and used to create a fairly narrow flow channel collocated with a 100 mV/m applied electric field (also the value used by *St.-Maurice and Schunk* [1981]).

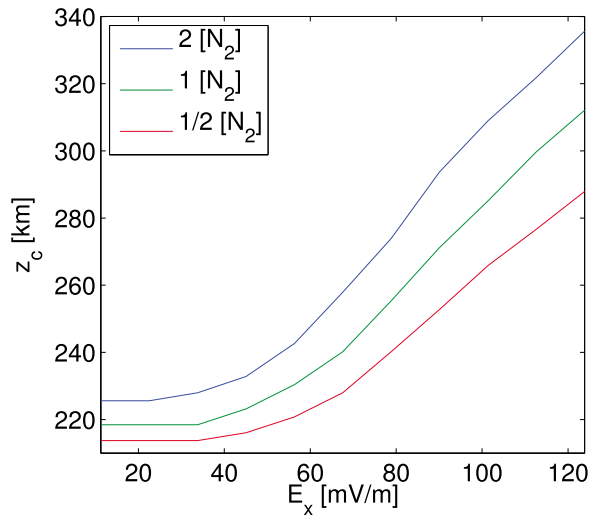

Figure 7. Dependence of ion composition on electric field and O/N_2.

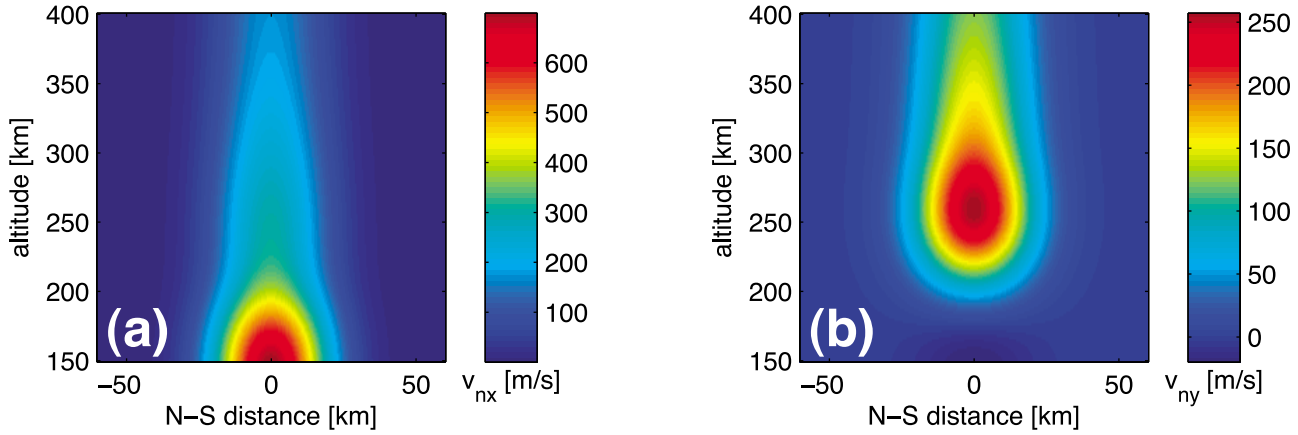

Figure 8. Horizontal neutral winds input into simulation (adapted from *St.-Maurice and Schunk* [1981]).

Both the field and wind values are attenuated toward the edge of the channel.

[40] Figure 9 shows the ionospheric model results displayed as profiles extracted from the center of the active region after 5 mins. of simulation time. Three simulation cases are shown in each panel, a quiescent profile, a profile with no wind and 100 mV/m field, and a profile with the structured winds of Figure 8 and 100 mV/m field. The effect of the structured winds is evident in average ion temperature in Figure 9a, while the composition and density profiles are affected to a much lesser degree. The change in the ion temperature profile shape illustrated in the simulations will most likely have a substantial effect on any attempts to estimate composition by modeling the temperature and fitting IS spectra for ion mass. This possibility has been mentioned in *Zettergren et al.* [2011], who have also suggested a novel Fabry-Perot interferometer experiment to untangle the effects of structured winds on frictional heating.

6. Consistency of Model Results With ISR Measurements

[41] The plasma redistribution and loss processes simulated in preceding sections are observable under certain assumptions via incoherent scatter radar. This affords an opportunity to check consistency with the directly estimated quantities and to evaluate plausibility of methods for indirect estimations.

[42] The ion upflow dealt with in this paper is of the type caused by intense frictional heating, so-called type-1 upflows [*Wahlund et al.*, 1992]. A large fraction of ion upflows observed at high altitudes contain at least some ion heating, and possibly electron heating, as well [*Ogawa et al.*, 2009]. Topside ionospheric fluxes exhibited in Figure 5a peak at $\sim$2–4 $\times$ 10^{13} for strong electron fields (70–120 mV/m) and are comparable to published ISR measurements of thermal ion upflow fluxes [*Semeter et al.*, 2003; *Zettergren et al.*, 2008; *Ogawa et al.*, 2009] (note that many of these measurements were combined type-1/type-2 events or had no apparent cause).

[43] It is usually not possible to directly estimate ion composition from high-latitude ISR measurements, but instead it is assumed in the spectral fitting routines. However, many attempts have been made to mitigate this issue by effectively adding information into the ISR spectral fitting routines [e.g., *Oliver*, 1979; *Kelly and Wickwar*, 1981; *Cabrit and Kofman*, 1997; *Litvine et al.*, 1998; *Shibata et al.*, 2000; *Lathuillere et al.*, 1983; *Haggstrom and Collis*, 1990; *Gaimard et al.*, 1996, and references therein]. Recent techniques for estimating molecular ions from ISR data have addressed auroral ionospheric temperature anisotropies and the need for short integration times to resolve the dynamic

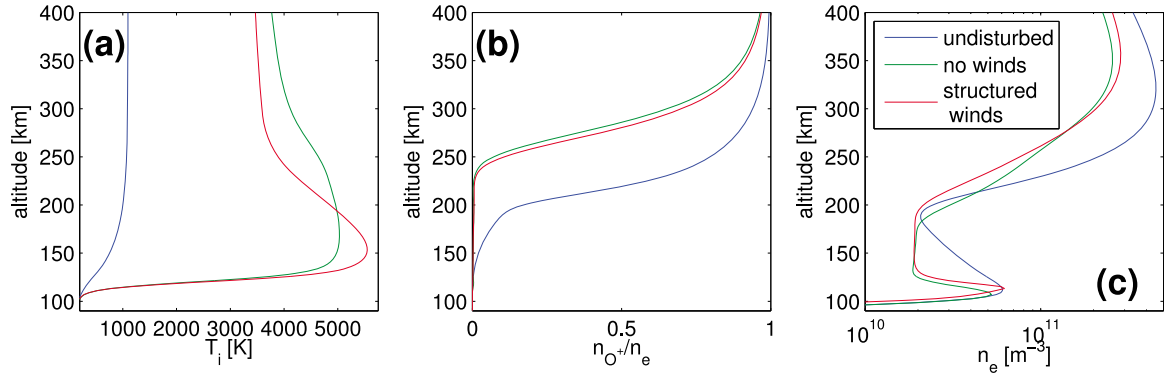

Figure 9. Effects of neutral wind structure on heating and composition. Profiles shown have been extracted from the center of the wind disturbance region.

nature of composition variability [*Blelly et al.*, 2010; *Zettergren et al.*, 2011]. Relevant to the current modeling studies, *Zettergren et al.* [2011] have presented several events of extreme frictional heating alongside estimates of large numbers of F-region molecular ions. Their analysis showed consistency between estimated crossover altitude (where the plasma is equal part atomic and molecular ions) dependence on applied electric field and numerical simulations with the TRANSCAR model [*Blelly et al.*, 1996; *Lilensten and Blelly*, 2002]. However, their analysis of 13 Nov. 2003 data indicated electric fields of ∼130 mV/m accompanied by crossover altitudes of ∼375 km (i.e., the plasma at the F-region peak was predominantly molecular!). These cases were not studied theoretically in their paper or its companion *Zettergren et al.* [2010], but can be examined with the model that we have developed. Specifically, the systematic analysis shown in Figure 5e shows that applied fields between 125–135 mV/m produce a crossover altitude of ∼350 km for background atmospheric conditions prescribed by MSIS. In light of the effects N_2 densities can have on crossover altitudes, the estimates of *Zettergren et al.* [2011], even in these extreme situations, are supported by the modeling work in this paper.

[44] Estimates of thermal molecular ion upflows have also been obtained by *Zettergren et al.* [2011], in their Figure 6. Their results indicate upward molecular fluxes of order 10^{13} occurring near the F-region peak in regions with driving fields of 80–100 mV/m. The model results of Figure 5b fall well short of this large value, by about a factor of 5. It is possible to obtain better agreement to the observed fluxes by increasing the N_2 density in the model, increasing the electric field, or by applying upward neutral winds. Even so the estimates from *Zettergren et al.* [2011] appear to be higher than what the model suggests - at least for the inferred heating conditions. It is not possible to make any more definitive claims regarding these estimates of molecular upflow by *Zettergren et al.* [2011], but the modeling does echo their main points that (1) large molecular fluxes are possible in auroral DCRs, and that (2) these regions are copious sources of molecular ions at high ionospheric altitudes. In fact, it is almost certain that these source regions form the seed population for outflowing molecular ions observed in the magnetosphere [*Peterson et al.*, 1994; *Lennartsson et al.*, 2000].

7. Summary and Conclusions

[45] A new two-dimensional model of the nighttime auroral ionosphere based on the 5-moment transport formulation and an electrostatic description of currents has been developed. The model self consistently calculates densities, drifts, and temperatures for 5 different positive ion species O^+, NO^+, N_2^+, O_2^+, N^+, each treated on equal footing, while also solving for the electric field in the ionosphere due to magnetospherically imposed boundary conditions or neutral wind dynamo effects. This model has been used to investigate the redistribution and loss of ionospheric plasma in auroral downward current regions due to synergistic effects of perpendicular to **B** transport, alterations in ion chemistry, thermal ion upflows, and *ad hoc* alterations in the neutral atmospheric winds and densities.

[46] The simulations presented here have shown that for strong magnetospheric forcing, ion heating and attendant chemistry changes play a substantial role in the formation of ionospheric depletions. For the cases examined, conversion of F-region plasma to molecular ions and subsequent recombination is more important than current closure loss to producing plasma depletions in the 250–400 km altitude ranges (as suggested by the limited analysis in *Zettergren et al.* [2010]). E-region depletion is entirely produced by the current closure loss process, which is also efficient at evacuating the lower F-region [*Doe et al.*, 1995]. The loss of plasma from the topside ionosphere is mostly due to the upflow generated by frictional heating and expansion. To our knowledge, this is the first detailed self-consistent modeling of the coupling of these important auroral ionospheric processes. This is important since some of the effects of frictional heating, particularly ion compositional changes, are extremely difficult to measure in an accurate way.

[47] The temporal features of plasma loss and transport have been shown to be highly dependent on the applied electric field. In particular the ionospheric response for all state variables has a shorter 'time constant' for stronger forcing. For typical strong arc-related electric fields, the E-region loss from the DCR occurs in 15–30 s, while the F-region depletion processes and topside upflows are somewhat slower (2–5 mins.).

[48] Both the modeled upflow and compositional changes are consistent with previous theoretical work (mostly based on 1-D modeling), and recent indirect observations of enhanced molecular ions due to auroral activity [*Blelly et al.*, 2010] and auroral arc disturbances [*Zettergren et al.*, 2011]. In particular, this work has demonstrated that auroral downward current regions can serve as source regions for outflowing molecular ions.

[49] Dynamics of the neutral atmosphere substantially alter the response of the ionosphere to auroral currents. Increases in N_2 density exaggerate the effect of frictional heating on F-region molecular ions. Furthermore, field aligned structure in the horizontal winds can produce very unusual spatial structure in ion frictional heating. This fact is particularly important when evaluating recently developed techniques for estimating ion composition from ISR data, which rely on the wind being constant through the F-region. In general, the modeling results highlight the need to account for variable composition in ISR analysis, since a wide variety of auroral processes have been shown to generate changes in composition. However, our analysis also demonstrates the difficulty in formulating a technique based on self-consistent modeling of ion temperature profiles.

[50] Future work will focus primarily on detailed model-data comparisons using imaging mode experiments from the PFISR and RISR radar systems [e.g., *Semeter et al.*, 2010]. Additional model extensions include self-consistent modeling of Alfven wave effects on the multi-species, collisional, chemically reactive ionospheric plasma. Furthermore, the model presented here will be extended to higher altitudes, and augmented to include H^+, dayside photoionization effects, and electron heating by precipitating suprathermal particles. Finally, there appears to be a need for more detailed analysis of the implications of neutral wind structure on estimation of molecular ions from ISR data.

[51] **Acknowledgments.** M.Z. acknowledges the support of NSF grant AGS-1000302 and ERAU internal grant 13267 for this research.

[52] Robert Lysak thanks Tomas Karlsson and another reviewer for their assistance in evaluating this paper.

References

Aikio, A., K. Mursula, S. Buchert, F. Forme, O. Amm, G. Marklund, M. Dunlop, D. Fontaine, A. Vaivads, and A. Fazakerley (2004), Temporal evolution of two auroral arcs as measured by the Cluster satellite and coordinated ground-based instruments, *Ann. Geophys.*, *22*, 4089–4101, doi:10.5194/angeo-22-4089-2004.

André, M., and A. W. Yau (1997), Theories and observations of ion energization and outflow in the high latitude magnetosphere, *Space Sci. Rev.*, *80*, 27–48.

André, M., P. Norqvist, L. Andersson, L. Eliasson, A. I. Eriksson, L. Blomberg, R. E. Erlandson, and J. Waldemark (1998), Ion energization mechanisms at 1700 km in the auroral region, *J. Geophys. Res.*, *103*, 4199–4222, doi:10.1029/97JA00855.

Banks, P. M., and T. E. Holzer (1969), High-latitude plasma transport: The polar wind, *J. Geophys. Res.*, *74*, 6317–6332.

Banks, P. M., and G. Kockarts (1973), *Aeronomy*, Academic, New York.

Blelly, P. L., and R. W. Schunk (1993), A comparative study of the time-dependent standard 8-, 13- and 16-moment transport formulations of the polar wind, *Ann. Geophys.*, *11*, 443–469.

Blelly, P.-L., A. Robineau, J. Lilensten, and D. Lummerzheim (1996), 8-moment fluid models of the terrestrial high-latitude ionosphere between 100 and 3000 km, in *Solar Terrestrial Energy Program: Handbook of Ionospheric Model*, edited by R. W. Schunk, pp. 53–72, Cent. for Atmos. and Space Sci., Utah State Univ., Logan, Utah.

Blelly, P.-L., D. Alcaydé, and A. P. van Eyken (2010), A new analysis method for determining polar ionosphere and upper atmosphere characteristics from ESR data: Illustration with IPY period, *J. Geophys. Res.*, *115*, A09322, doi:10.1029/2009JA014876.

Butler, T. W., J. Semeter, C. J. Heinselman, and M. J. Nicolls (2010), Imaging F region drifts using monostatic phased-array incoherent scatter radar, *Radio Sci.*, *45*, RS5013, doi:10.1029/2010RS004364.

Cabrit, B., and W. Kofman (1997), Ionospheric composition measurement by EISCAT using a global fit procedure, *Ann. Geophys.*, *14*, 1496–1505, doi:10.1007/s00585-996-1496-2.

Cran-McGreehin, A. P., A. N. Wright, and A. W. Hood (2007), Ionospheric depletion in auroral downward currents, *J. Geophys. Res.*, *112*, A10309, doi:10.1029/2007JA012350.

de Boer, J. D., J.-M. A. Noël, and J.-P. St.-Maurice (2010), The effects of mesoscale regions of precipitation on the ionospheric dynamics, electrodynamics and electron density in the presence of strong ambient electric fields, *Ann. Geophys.*, *28*, 1345–1360, doi:10.5194/angeo-28-1345-2010.

de La Beaujardiere, O., R. Vondrak, and M. Baron (1977), Radar observations of electric fields and currents associated with auroral arcs, *J. Geophys. Res.*, *82*, 5051–5062, doi:10.1029/JA082i032p05051.

Diloy, P.-Y., A. Robineau, J. Lilensten, P.-L. Blelly, and J. Fontanari (1996), A numerical model of the ionosphere, including the E-region above EISCAT, *Ann. Geophys.*, *14*, 191–200.

Doe, R. A., M. Mendillo, J. F. Vickrey, L. J. Zanetti, and R. W. Eastes (1993), Observations of nightside auroral cavities, *J. Geophys. Res.*, *98*, 293–310, doi:10.1029/92JA02004.

Doe, R. A., J. F. Vickrey, and M. Mendillo (1995), Electrodynamic model for the formation of auroral ionospheric cavities, *J. Geophys. Res.*, *100*, 9683–9696, doi:10.1029/95JA00001.

Evans, D. S., N. C. Maynard, J. Troim, T. Jacobsen, and A. Egeland (1977), Auroral vector electric field and particle comparisons: 2. Electrodynamics of an arc, *J. Geophys. Res.*, *82*, 2235–2249.

Gaimard, P., C. Lathuillere, and D. Hubert (1996), Non-Maxwellian studies in the auroral F region: A new analysis of incoherent scatter spectra, *J. Atmos. Terr. Phys.*, *58*, 415–433.

Ganguli, S. B. (1996), The polar wind, *Rev. Geophys.*, *34*, 311–348, doi:10.1029/96RG00497.

Haggstrom, I., and P. N. Collis (1990), Ion composition changes during F-region density depletions in the presence of electric fields at auroral latitudes, *J. Atmos. Terr. Phys.*, *52*, 519–529.

Huba, J. D., G. Joyce, and J. A. Fedder (2000), Sami2 is Another Model of the Ionosphere (SAMI2): A new low-latitude ionosphere model, *J. Geophys. Res.*, *105*, 23,035–23,054, doi:10.1029/2000JA000035.

Johnson, M. L., J. S. Murphree, G. T. Marklund, and T. Karlsson (1998), Progress on relating optical auroral forms and electric field patterns, *J. Geophys. Res.*, *103*, 4271–4284, doi:10.1029/97JA00854.

Karlsson, T., G. Marklund, N. Brenning, and I. Axnas (2005), On Enhanced Aurora and Low-Altitude Parallel Electric Fields, *Phys. Scr.*, *72*, 419–422, doi:10.1238/Physica.Regular.072a00419.

Kelly, J. D., and V. B. Wickwar (1981), Radar measurements of high-latitude ion composition between 140 and 300 km altitude, *J. Geophys. Res.*, *86*, 7617–7626.

Lathuillère, C., and W. Kofman (2006), A short review on the F1-region ion composition in the auroral and polar ionosphere, *Adv. Space Res.*, *37*, 913–918, doi:10.1016/j.asr.2005.12.014.

Lathuillere, C., G. Lejeune, and W. Kofman (1983), Direct measurements of ion composition with EISCAT in the high-latitude F1 region, *Radio Sci.*, *18*, 887–893.

Lennartsson, O. W., H. L. Collin, A. G. Ghielmetti, and W. K. Peterson (2000), A statistical comparison of the outflow of N_2^+, NO^+ and O_2^+ molecular ions with that of atomic O^+ ions using Polar/TIMAS observations, *J. Atmos. Sol. Terr. Phys.*, *62*, 477–483, doi:10.1016/S1364-6826(00)00019-5.

Lilensten, J., and P.-L. Blelly (2002), The TEC and F2 parameters are tracers of the ionosphere and thermosphere, *J. Atmos. Sol. Terr. Phys.*, *64*, 775–793.

Litvine, A., W. Kofman, and B. Cabrit (1998), Ion composition measurements and modelling at altitudes from 140 to 350 km using EISCAT measurements, *Ann. Geophys.*, *16*, 1159–1168.

Lotko, W. (2004), Inductive magnetosphere-ionosphere coupling, *J. Atmos. Sol. Terr. Phys.*, *66*, 1443–1456, doi:10.1016/j.jastp.2004.03.027.

Lynch, K. A., J. L. Semeter, M. Zettergren, P. Kintner, R. Arnoldy, E. A. MacDonald, E. Klatt, J. LaBelle, and M. Samara (2007), Auroral ion outflow: Low altitude energization, *Ann. Geophys.*, *25*, 1967–1977.

Lysak, R. L., and Y. Song (2002), Energetics of the ionospheric feedback interaction, *J. Geophys. Res.*, *107*(A8), 1160, doi:10.1029/2001JA000308.

Marklund, G. (1984), Auroral arc classification scheme based on the observed arc-associated electric field pattern, *Planet. Space Sci.*, *32*, 193–211, doi:10.1016/0032-0633(84)90154-5.

McFadden, J. P., et al. (1998), Spatial structure and gradients of ion beams observed by FAST, *Geophys. Res. Lett.*, *25*, 2021–2024, doi:10.1029/98GL00648.

McFarland, M., D. L. Albritton, F. C. Fehsenfeld, E. E. Ferguson, and A. L. Schmeltekopf (1973), Flow-drift technique for ion mobility and ion-molecule reaction rate constant measurements. II. Positive ion reactions of N^+, O^+, and H_2^+ with O_2 and O^+ with N_2 from thermal to ~2 eV, *J. Chem. Phys.*, *59*, 6620–6628.

Moore, T. E., and J. L. Horwitz (2007), Stellar ablation of planetary atmospheres, *Rev. Geophys.*, *45*, RG3002, doi:10.1029/2005RG000194.

Moore, T. E., R. Lundin, D. Alcayde, M. André, S. B. Ganguli, M. Temerin, and A. Yau (1999), Source processes in the high-latitude ionosphere, *Space Science Reviews*, *88*, 7–84, doi:10.1023/A:1005299616446.

Noël, J.-M. A., J.-P. St.-Maurice, and P.-L. Blelly (2000), Nonlinear model of short-scale electrodynamics in the auroral ionosphere, *Ann. Geophys.*, *18*, 1128–1144.

Noël, J.-M. A., J.-P. S.-Maurice, and P.-L. Blelly (2005), The effect of E-region wave heating on electrodynamical structures, *Ann. Geophys.*, *23*, 2081–2094, doi:10.5194/angeo-23-2081-2005.

Ogawa, Y., et al. (2008), Coordinated EISCAT Svalbard radar and Reimei satellite observations of ion upflows and suprathermal ions, *J. Geophys. Res.*, *113*, A05306, doi:10.1029/2007JA012791.

Ogawa, Y., S. C. Buchert, R. Fujii, S. Nozawa, and A. P. van Eyken (2009), Characteristics of ion upflow and downflow observed with the European Incoherent Scatter Svalbard radar, *J. Geophys. Res.*, *114*, A05305, doi:10.1029/2008JA013817.

Oliver, W. L. (1979), Incoherent scatter radar studies of the daytime middle thermosphere, *Ann. Geophys.*, *35*, 121–139.

Opgenoorth, H. J., I. Haggstrom, P. J. S. Williams, and G. O. L. Jones (1990), Regions of strongly enhanced perpendicular electric fields adjacent to auroral arcs, *J. Atmos. Terr. Phys.*, *52*, 449–458.

Peterson, W. K., et al. (1994), On the sources of energization of molecular ions at ionospheric altitudes, *J. Geophys. Res.*, *99*, 23,257–23,274.

Picone, J. M., A. E. Hedin, D. P. Drob, and A. C. Aikin (2002), NRLMSISE-00 empirical model of the atmosphere: Statistical comparisons and scientific issues, *J. Geophys. Res.*, *107*(A12), 1468, doi:10.1029/2002JA009430.

Rees, M. H. (1989), *Physics and Chemistry of the Upper Atmosphere*, Cambridge Univ. Press. Cambridge, U. K.

Richards, P. G. (1995), Effects of auroral electron precipitation on topside ion ouflows, in *Cross-Scale Coupling in Space Plasma*, *Geophys. Monogr. Ser.*, vol. 93, edited by J. L. Horwitz, N. Singh, and J. L. Burch, pp. 121–126, AGU, Washington, D. C.

Russell, A. J. B., A. N. Wright, and A. W. Hood (2010), Self-consistent ionospheric plasma density modifications by field-aligned currents: Steady state solutions, *J. Geophys. Res.*, *115*, A04216, doi:10.1029/2009JA014836.

Schunk, R. W. (1977), Mathematical structure of transport equations for multispecies flows, *Rev. Geophys.*, *15*, 429–445.

Schunk, R. W. (2000), Theoretical developments on the causes of ionospheric outflow, *J. Atmos. Sol. Terr. Phys.*, *62*, 399–420.

Schunk, R. W., and A. F. Nagy (1978), Electron temperatures in the *F* region of the ionosphere: Theory and observations, *Rev. Geophys.*, *16*, 355–399.

Schunk, R. W., P. M. Banks, and W. J. Raitt (1975), Effect of electric fields on the daytime high-latitude E and F regions, *J. Geophys. Res.*, *80*, 3121–3130.

Semeter, J., and F. Kamalabadi (2005), Determination of primary electron spectra from incoherent scatter radar measurements of the auroral *E* region, *Radio Sci.*, *40*, RS2006, doi:10.1029/2004RS003042.

Semeter, J., C. J. Heinselman, J. P. Thayer, R. A. Doe, and H. U. Frey (2003), Ion upflow enhanced by drifting *F*-region plasma structure along the nightside polar cap boundary, *Geophys. Res. Lett.*, *30*(22), 2139, doi:10.1029/2003GL017747.

Semeter, J., T. Butler, C. Heinselman, M. Nicolls, J. Kelly, and D. Hampton (2009), Volumetric imaging of the auroral ionosphere: Initial results from PFISR, *J. Atmos. Sol. Terr. Phys.*, *71*, 738–743, doi:10.1016/j.jastp.2008.08.014.

Semeter, J., T. W. Butler, M. Zettergren, C. J. Heinselman, and M. J. Nicolls (2010), Composite imaging of auroral forms and convective flows during a substorm cycle, *J. Geophys. Res.*, *115*, A08308, doi:10.1029/2009JA014931.

Shibata, T., H. Matsuya, and J. Hoashi (2000), Ion composition in the auroral lower F-region inferred from residuals of ion temperature profiles observed with EISCAT, *Adv. Space Res.*, *25*, 201–210, doi:10.1016/S0273-1177(99)00919-9.

St.-Maurice, J.-P., and P. J. Laneville (1998), Reaction rate of O^+ with O_2, N_2, and NO under highly disturbed auroral conditions, *J. Geophys. Res.*, *103*, 17,519–17,522.

St.-Maurice, J.-P., and R. W. Schunk (1981), Ion-neutral momentum coupling near discrete high-latitude ionospheric features, *J. Geophys. Res.*, *86*, 11,299–11,321.

St.-Maurice, J.-P., and D. G. Torr (1978), Nonthermal rate coefficients in the ionosphere: The reactions of O^+ with N_2, O_2, and NO, *J. Geophys. Res.*, *83*, 969–977, doi:10.1029/JA083iA03p00969.

St.-Maurice, J.-P., W. Kofman, and D. James (1996), In situ generation of intense parallel electric fields in the lower ionosphere, *J. Geophys. Res.*, *101*, 335–356, doi:10.1029/95JA02586.

Streltsov, A. V., and W. Lotko (2004), Multiscale electrodynamics of the ionosphere-magnetosphere system, *J. Geophys. Res.*, *109*, A09214, doi:10.1029/2004JA010457.

Streltsov, A. V., and W. Lotko (2008), Coupling between density structures, electromagnetic waves and ionospheric feedback in the auroral zone, *J. Geophys. Res.*, *113*, A05212, doi:10.1029/2007JA012594.

Strickland, D. J., R. J. Cox, R. R. Meier, and D. P. Drob (1999), Global O/N_2 derived from DE 1 FUV dayglow data: Technique and examples from two storm periods, *J. Geophys. Res.*, *104*, 4251–4266, doi:10.1029/98JA02817.

Torr, M. R., D. G. Torr, and J. P. Saint-Maurice (1977), The rate coefficient for the $O^+ + N_2$ reaction in the ionosphere, *J. Geophys. Res.*, *82*, 3287–3290.

Wahlund, J.-E., H. J. Opgenoorth, I. Häggström, K. J. Winser, and G. O. L. Jones (1992), EISCAT observations of topside ionospheric ion outflows during auroral activity: Revisited, *J. Geophys. Res.*, *97*, 3019–3037.

Yau, A. W., and M. André (1997), Sources of ion outflow in the high latitude ionosphere, *Space Sci. Rev.*, *80*, 1–25.

Zettergren, M., J. Semeter, P.-L. Blelly, and M. Diaz (2007), Optical estimation of auroral ion upflow: Theory, *J. Geophys. Res.*, *112*, A12310, doi:10.1029/2007JA012691.

Zettergren, M., J. Semeter, P.-L. Blelly, G. Sivjee, I. Azeem, S. Mende, H. Gleisner, M. Diaz, and O. Witasse (2008), Optical estimation of auroral ion upflow: 2. A case study, *J. Geophys. Res.*, *113*, A07308, doi:10.1029/2008JA013135.

Zettergren, M., J. Semeter, B. Burnett, W. Oliver, C. Heinselman, P. Blelly, and M. Diaz (2010), Dynamic variability in F-region ionospheric composition at auroral arc boundaries, *Ann. Geophys.*, *28*, 651–664.

Zettergren, M., J. Semeter, C. Heinselman, and M. Diaz (2011), Incoherent scatter radar estimation of *F* region ionospheric composition during frictional heating events, *J. Geophys. Res.*, *116*, A01318, doi:10.1029/2010JA016035.

Zhu, H., A. Otto, D. Lummerzheim, M. H. Rees, and B. S. Lanchester (2001), Ionosphere-magnetosphere simulation of small-scale structure and dynamics, *J. Geophys. Res.*, *106*, 1795–1806, doi:10.1029/1999JA000291.